EVALUATING THE ROLE OF TRIP WIRE DIAMETER IN THE DEVELOPMENT OF RESTRICTED NONLINEAR BOUNDARY LAYERS

Alexandra C. Risha
Dept. of Mechanical Eng.
Johns Hopkins University
3400 N. Charles St.
Baltimore, MD, 21218, USA
arisha1@jh.edu

Benjamin A. Minnick
Maneuvering and Control Division
Naval Surface Warfare Center
9500 MacArthur Blvd.
West Bethesda, MD, 20817, USA
benjamin.a.minnick.civ@us.navy.mil

Dennice F. Gayme
Dept. of Mechanical Eng.
Johns Hopkins University
3400 N. Charles St.
Baltimore, MD, 21218, USA
dennice@jhu.edu

ABSTRACT

This study employs restricted nonlinear wall-resolved large eddy simulations (RNL-WRLES) to explore the influence of trip wire size on boundary layer development over a moving wall. An imposed momentum deficit is used to model the effect of wall-mounted trip elements of varying diameters. Comparisons to direct numerical simulations (DNS) indicate that RNL-WRLES transition to turbulence at a later time, but the asymptotic behavior of integral quantities follow DNS trends. The mean velocity profile and Reynolds stresses collapse in the near-wall region across trip conditions, while outer-layer differences diminish as the flow evolves toward fully developed turbulence. Larger trip diameter intensifies early flow excitation in the outer region, thickening the boundary layers. RNL-WLRES match statistical trends from DNS for different trip diameters at those from experiments at fixed momentum Reynolds numbers and time instances. These findings support the RNL framework as a computationally tractable approach for investigating the mechanisms governing boundary layer evolution under varying trip wire effects.

INTRODUCTION

The near surface dynamics of developing boundary layers affect system efficiency across a range of applications. The evolution of these flows can be greatly influenced by how transition to turbulence is initiated (tripped). Physical tripping mechanisms in experimental studies include rods and sandpaper used to disturb the flow field and initiate transition e.g., Marusic et al. (2015); Park et al. (2024); Tang et al. (2024). In simulations, initial velocity profiles are used to model the behavior of these elements see e.g., Schlatter & Örlü (2012); Kozul et al. (2016); Watanabe et al. (2019). This flow excitation can lead to long lasting changes to the flow behavior that persist for long times and distances downstream. For example, certain tripping modalities have been shown to "artificially thicken" the boundary layer which influences flow properties and can lead to higher Reynolds number behavior that is not consistent with the actual flow (e.g., see Marusic et al. (2015); Tang et al. (2024) and references therein). Obtaining flow behavior independent of trip modality can therefore require long inflow regions for studying spatially developing boundary layers (Schlatter & Örlü, 2012; Marusic et al., 2015).

This need for long computational domains to study the evolution of spatially developing boundary layers can be mitigating by instead using a temporally developing framework. Flow over a wall moving at constant velocity, for example, can be related to zero pressure gradient (ZPG) boundary layers through a coordinate system change. This approach has been shown to produce statistics and integral quantities comparable to those observed in experimental and numerical studies of spatially developing flows (Kozul et al., 2016; Watanabe et al., 2019). It reduces computational complexity by imposing the streamwise periodicity of canonical flows, thereby eliminating the need for the recycling methods typically required to simulate spatially developing boundary layers (Kozul et al., 2016; Watanabe et al., 2019).

A temporally developing configuration was previously used to study the effect of trip diameter modeled as a hyperbolic tangent initial velocity profile with varying magnitude using direct numerical simulations (DNS) (Kozul et al. (2016); Watanabe et al. (2019)). In this work, we perform a similar study but further improve computational tractability by using a reduced order model of the flow evolution. We employ the restricted nonlinear (RNL) model (Thomas et al., 2015; Bretheim et al., 2018; Gayme & Minnick, 2019) because it emphasizes streamwise-coherent dynamics, providing a natural and efficient representation for temporally developing flows. This approach reduces computational cost by imposing a dynamical restriction that limits nonlinear interactions to those contributing to the streamwise-averaged mean flow (i.e., the $k_x = 0$ mode in a Fourier decomposition; see, e.g., Bretheim et al. (2018)). Minnick & Gayme (2024) and Risha et al. (2026) previously used the RNL model to investigate the evolution of turbulent statistical and integral quantities with temporal development of the boundary layer.

We perform RNL wall-resolved large eddy simulations (WRLES) for varying trip conditions that are modeled following the approach in Kozul et al. (2016). Instantaneous snapshots of the velocity field, mean velocity profiles, and skin friction coefficients through the laminar-to-turbulent transitional region within the boundary layer are used to quantify the effect of trip diameter on the resulting flow field. Comparisons of the RNL-WRLES results with those from direct numerical simulation (DNS) indicate that the RNL framework reproduces the expected increases in early flow excitation in the outer region, thickening the boundary layers as the trip Reynolds number increases. At a fixed trip diameter, we observed the expected collapse in the velocity field and the Reynolds stress trends as the momentum thickness Reynolds number increases. Together these results provide evidence that the RNL-WRLES provides a computationally tractable representation of a developing boundary layer suitable for such parametric studies.

METHODOLOGY

We consider flow over a wall where (x,y,z) are the respective streamwise, wall-normal, and spanwise components. A temporal boundary layer is developed by impulsively moving a wall at speed U_w. The initial flow field $\boldsymbol{u_0} = (u_0, v_0, w_0)$ consists of a base velocity profile and a fluctuating component, i.e., $\boldsymbol{u_0} = \overline{\boldsymbol{u_0}} + \boldsymbol{u'_0}$. Following Kozul et al. (2016), the streamwise velocity component of the base profile consists of a hyperbolic tangent function,

$$\overline{u_0} = \frac{U_w}{2} + \frac{U_w}{2}\tanh\left[\frac{D}{2\theta_{sl}}(1-\frac{y}{D})\right] \tag{1}$$

and $(\overline{v_0} = \overline{w_0} = 0)$, which models the momentum deficit developed in the wake of a wall-mounted trip wire. This profile depends on a trip wire diameter, D, the momentum thickness of the shear layer, $\theta_{sl} = \frac{54\nu}{U_w}$, and kinematic viscosity, ν, which are used to define a trip Reynolds number $Re_D = \frac{DU_w}{\nu}$. In addition to the trip function forcing (1), transition is promoted through the addition of small amplitude white noise ($< 0.1U_w$) to all fluctuating velocity components (i.e., $\boldsymbol{u'_0}$) at a near wall-normal height, $y < \delta_0$, and in regions where the difference between the wall velocity and the streamwise local mean initial flow, $(U_w - \overline{u_0})$, is less than $10^{-2}U_w$. We employ this δ_0 as the characteristic length scale used for normalization (Minnick & Gayme, 2024).

The restricted nonlinear large eddy simulation (RNL-LES) equations are derived by decomposing the total filtered flow field, $\widetilde{\mathbf{u}}_T(x,y,z,t)$, into a large-scale streamwise-averaged mean, $\widetilde{\mathbf{U}}(y,z,t) = \langle \widetilde{\mathbf{u}}_T \rangle_x$, and small-scale streamwise-varying perturbations about this mean, $\widetilde{\mathbf{u}}(x,y,z,t)$, i.e., $\widetilde{\mathbf{u}}_T = \widetilde{\mathbf{U}} + \widetilde{\mathbf{u}}$, where t is time. Brackets with a subscript indicate averaging in the direction indicated. An analogous decomposition is applied for the total filtered pressure field, $\widetilde{p}_T$. The resulting mean and perturbation dynamics are

$$\partial_t \widetilde{\mathbf{U}} + \widetilde{\mathbf{U}} \cdot \nabla \widetilde{\mathbf{U}} + \rho^{-1}\nabla \widetilde{P} + \nabla \cdot \langle \tau \rangle_x = -\langle \widetilde{\mathbf{u}} \cdot \nabla \widetilde{\mathbf{u}} \rangle_x \tag{2}$$

$$\partial_t \widetilde{\mathbf{u}} + \widetilde{\mathbf{u}} \cdot \nabla \widetilde{\mathbf{U}} + \widetilde{\mathbf{U}} \cdot \nabla \widetilde{\mathbf{u}} + \rho^{-1}\nabla \widetilde{p} + \nabla \cdot \left(\tau - \langle \tau \rangle_x\right) = 0, \tag{3}$$

and $\nabla \cdot \widetilde{\mathbf{U}} = \nabla \cdot \widetilde{\mathbf{u}} = 0$, where ρ is density, and τ is a streamwise dependent subgrid scale tensor. The RNL equations differ from the Navier Stokes equations in that $-(\widetilde{\mathbf{u}} \cdot \nabla \widetilde{\mathbf{u}} - \langle \widetilde{\mathbf{u}} \cdot \nabla \widetilde{\mathbf{u}} \rangle_x)$, i.e., nonlinear perturbation-perturbation interactions not contributing to the large-scale are omitted (while full-nonlinear interactions between spanwise scales are maintained). Further order reduction is achieved by limiting the streamwise wave number support of the dynamics (Bretheim et al., 2018). Boundary conditions include no slip and no penetration at the wall, and no stress at the top of the domain. Periodic boundary conditions are enforced in the streamwise and spanwise directions. In the discussion that follows, the tilde indicating filtered flow variables will be omitted to simplify notation.

Equations (2) and (3) are solved in a modified version of the Johns Hopkins LESGO code (https://lesgo.me.jhu.edu) using the wall-adapting local eddy-viscosity (WALE) subgrid stress model from Nicoud & Ducros (1999). Due to the reduced RNL streamwise dynamics, a streamwise constant eddy viscosity operator is assumed, which requires the use of a higher model coefficient $C_w = 0.467$ (Bretheim et al., 2018; Risha et al., 2026). A non-uniform hyperbolic tangent stretching function is used to define the wall-normal grid. The wall-normal height is selected to ensure that it is at least two times greater than the final boundary layer thickness at the final simulation time, $\delta_f(t_f)$ and a max grid stretch of 2.9% is maintained. The domain extents are $L_y/\delta_0 = 9, L_z/\delta_0 = 3\pi$. During the simulation, a minimum of 5 points remain below $y^+ < 5$ and $\Delta z^+ = 7 - 26$. The $+$ indicates inner unit scaling i.e., $\delta_\nu = u_\tau/\nu$ where $u_\tau = \sqrt{\tau_w/\rho}$ is the friction velocity and τ_w is the wall shear stress. The RNL model does not have a physical streamwise grid, instead streamwise derivatives are computed in Fourier space and the nonlinear term is computed as a convolution (see Bretheim et al. (2018) for details of the implementation). The perturbation dynamics are supported by streamwise-varying modes $k_x\delta_0 = 6, 7, 8$, (and the streamwise mean mode $k_x\delta_0 = 0$), where $k_x = n\frac{2\pi}{L_x}$ is the dimensional wave number, n is a non-negative integer, and L_x is a surrogate streamwise domain extent. The wave numbers were selected to match the mean profile and log-law indicator function at varying Reynolds numbers when compared to DNS. They also produced a secondary peak in the outer layer of the energy spectra (shown in Risha et al. (2026)). While the dynamics can sustain on a single streamwise-varying mode, we select three wave numbers to enable interactions among a broader range of streamwise scales.

As in prior studies (Kozul et al., 2016; Watanabe et al., 2019), we use a moving wall frame of reference (i.e., $U_w - u_T$) in order to directly compare results to those of a spatially developing flows. We can then define a temporal Reynolds number, $Re_t = U_w^2 t/\nu$, which is equivalent to Re_X in Kozul et al. (2016) through a change of coordinates $X = U_w t$, where X is the streamwise downstream position. We then define the corresponding momentum thickness $\theta = \int_0^\infty \frac{\langle u_T \rangle}{U_w}\left(1 - \frac{\langle u_T \rangle}{U_w}\right) dy$, displacement thickness $\delta^* = \int_0^\infty \frac{\langle u_T \rangle}{U_w} dy$, and boundary layer thickness $\delta_{99} = 1 - \frac{\langle u_T \rangle}{U_w} = 0.99$. The shape factor is given by $H = \delta^*/\theta$.

RESULTS AND DISCUSSION

RNL-WRLES are carried out for five trip diameters associated with $Re_D = 250, 500, 1000, 1500$, and 2000. The computational tractability of the RNL framework enables statistical averaging over 100 temporally-ensembled realizations.

Figure 1 shows the cross-plane instantaneous streamwise component of the velocity normalized by the wall velocity, i.e., u_T/U_w, for each Re_D value at an early time $Re_t = 4.4 \times 10^5$ (top) and a later time $Re_t = 17.6 \times 10^5$ (bottom) in the boundary layer development. The trip wire diameter is observed to significantly influence boundary layer growth. As Re_D increases, the boundary layer exhibits enhanced growth at early times, which is consistent with the larger wake generated by increasing trip diameter. Tang et al. (2024) similarly reported that larger diameter wall-mounted cylinders (in their experiments), generated thicker spatial boundary layers at a respective downstream streamwise location. The amplified trip wire wake promotes an extended transitional region and facilitates an earlier onset of turbulence through intensified mixing. At the later time, the boundary layer thickness across the range of Re_D becomes comparatively uniform, indicating an approach toward a fully developed turbulent state that is independent of the initial conditions.

Figure 2 presents the skin friction coefficient, c_f, as a function of (a) the momentum thickness Reynolds number $Re_\theta = U_w\theta/\nu$, (b) the displacement thickness Reynolds num-

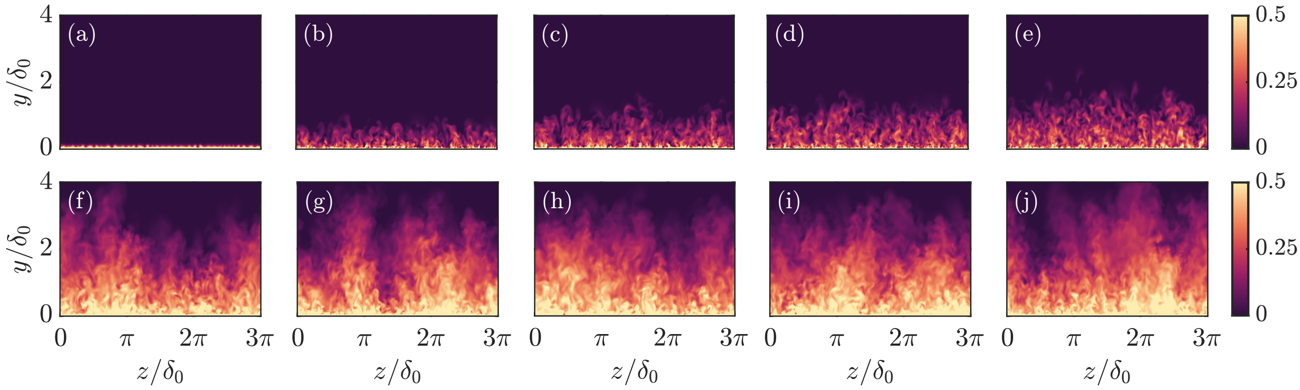

Figure 1. Cross-plane *(yz)* snapshots of the streamwise component of the velocity normalized by the wall velocity i.e., u_T/U_w for (a,f) $Re_D = 250$, (b,g) $Re_D = 500$, (c,h) $Re_D = 1000$, (d,i) $Re_D = 1500$, and (e,j) $Re_D = 2000$ at (a-e) $Re_t = 2.6\times10^5$ and (f-j) $Re_t = 41.8\times10^5$. Wall-normal domain is cropped for visualization purposes.

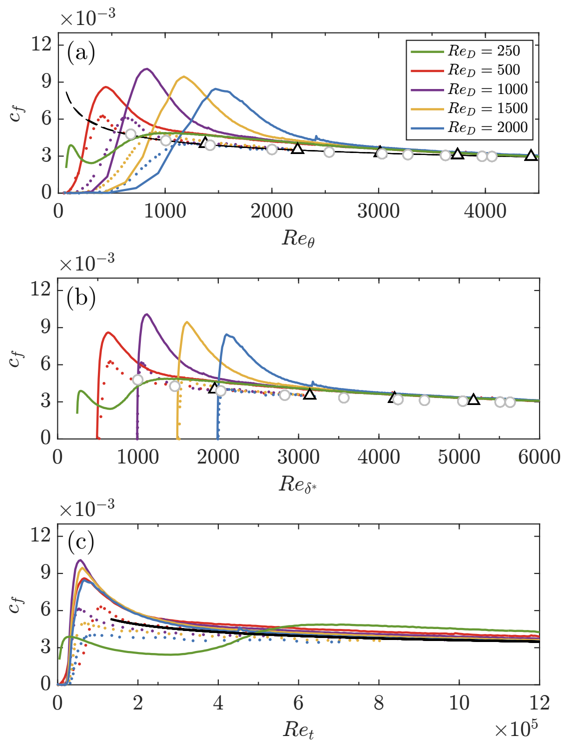

Figure 2. Skin friction coefficient $c_f = u_\tau^2/(0.5U_w^2)$ as a function of the (a) momentum thickness Reynolds number, (b) displacement thickness Reynolds number, and (c) temporal Reynolds number for RNL-WRLES $Re_D = 250$ (——), $Re_D = 500$ (——), $Re_D = 1000$ (——), $Re_D = 1500$ (——), and $Re_D = 2000$ (——). Dots indicate temporally-developing boundary layer DNS data from Kozul et al. (2016) (same color scheme). Symbols indicate spatially developing boundary layer DNS/LES data from Schlatter et al. (2010)(○) and Eitel-Amor et al. (2014)(△). Thin dashed line indicates $c_{f,turb} = 0.024Re_\theta^{-1/4}$ from Smits et al. (1983). Solid black line indicates resistive law from Kozul et al. (2016) where $Re_t = C_1 e^{\kappa[U_w^+ - \phi(1)]}\left[\left(U_w^+\right)^2 - \frac{2U_w^+}{\kappa} + \frac{2}{\kappa^2}\right] - \frac{2}{\kappa^2}C_1 e^{-\kappa\phi(1)}$ and $C_1 = 4.05$, $\phi(1) = 7.1$, and $\kappa = 0.384$.

ber $Re_{\delta^*} = \delta^* U_w/\nu$, and (c) Re_t for the five values of Re_D. The RNL-WRLES predictions (solid colored lines) are compared with theoretical expressions from Kozul et al. (2016) (solid black line) and Smits et al. (1983) (dashed black line), as well as DNS from Kozul et al. (2016) (colored dots), and DNS of a spatially developing ZPG boundary layer from Schlatter & Örlü (2012) (circle symbols) and Eitel-Amor et al. (2014) (triangle symbols). All of the RNL-WRLES achieve a turbulent state, even the $Re_D = 250$ case which did not transition to turbulence in the DNS study of Kozul et al. (2016). This is not unexpected as prior studies indicate larger turbulent kinetic energy and a higher production rate in RNL simulations versus DNS, see e.g., Gayme & Minnick (2019); Minnick & Gayme (2024), which could enable the flow to transition with lower energy input. Figure 2 also demonstrates that RNL-WRLES simulations show delayed transition compared to DNS Kozul et al. (2016). Prior RNL studies indicate streamwise-varying interactions control the onset of transition, while cross-stream interactions dominate subsequent evolution (Minnick & Gayme, 2024). Therefore, the dynamical restriction to three streamwise varying modes likely affects the transition time. From the integral momentum balance for a temporally developing boundary layer, the skin-friction coefficient is approximately proportional to the temporal rate of change of the displacement thickness, δ^*, rather than the momentum thickness, θ (as in spatially developing flows). This distinction explains the improved collapse observed in figure 2(b) (Kozul et al., 2016; Minnick & Gayme, 2024). All trip conditions attain a peak at similar Re_t and rapidly approach the asymptotic relations derived in Kozul et al. (2016), indicating that the initial perturbation does not significantly alter the long-time evolution of c_f. However, a perfect collapse of the profiles is not achieved, consistent with Kozul et al. (2016), since the flow development does not commence at precisely the same initial time (at the same location in a spatially developing framework).

Figure 3 shows (a) Re_τ, (b) Re_{δ^*}, (c) Re_t, and (d) H as a function of momentum thickness Reynolds for all of the Re_D values considered. The RNL-WRLES simulations exhibit a smaller slope in the Re_τ–Re_θ relationship compared to DNS trends, which would extrapolate to a higher deviation with increasing Reynolds number. While the agreement remains adequate in the Reynolds number range shown, the expected increasing error as Reynolds number increases is consistent with previous studies indicating that the RNL model accurately reproduces statistical behavior for low-to-moderate Reynolds numbers but that the accuracy diminishes with increasing Reynolds numbers (Minnick et al., 2023). The RNL-WRLES displacement thickness Reynolds number trends shown in fig-

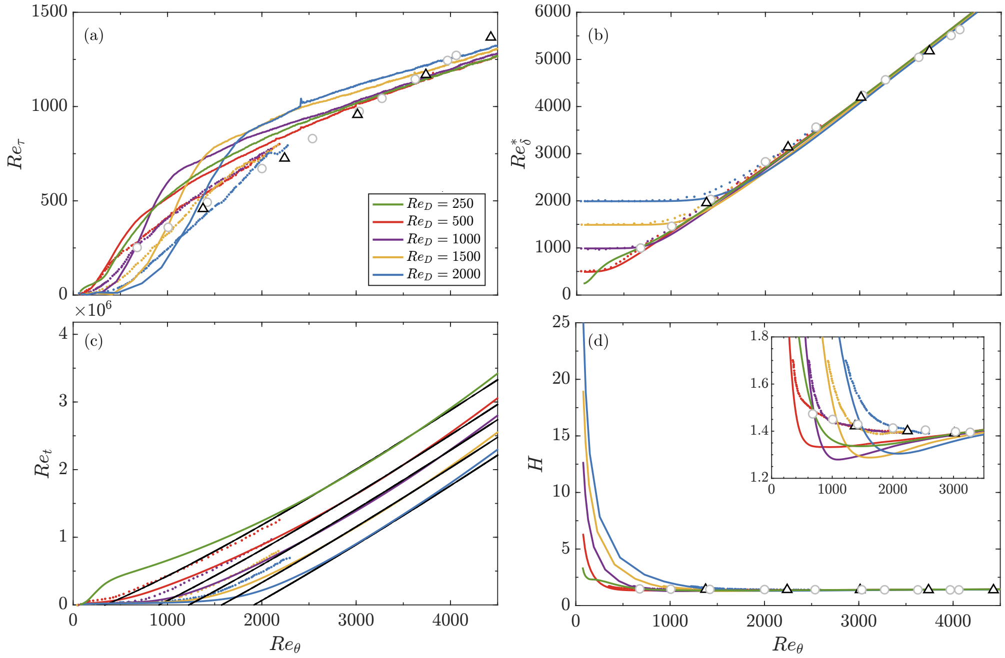

Figure 3. Evolution profiles of the (a) frictional Reynolds number, (b) displacement thickness Reynolds number, (c) temporal Reynolds number, and (d) shape factor as a function of the momentum thickness Reynolds number for all Re_D. See figure 2 caption for legend details.

ure 3(b) agree well with DNS data within the low-to-moderate Reynolds number regime highlighted here. Figure 3(c) confirms the later transition in the RNL-WRLES simulations versus DNS that was observed in Figure 2. The offset in the trends is due to the fact that the virtual-origin shift appears at larger Re_t versus the DNS data Kozul et al. (2016); however, the slope of the RNL-WRLES results remains consistent with the derived theoretical relation. The Re_t–Re_θ relationship also indicates that, for a fixed Re_X (time or analogously streamwise location in a spatially developing flow) during the transient phase, the boundary layer thickens (with correspondingly larger momentum and displacement thicknesses), corresponding to a larger trip diameter. This behavior is consistent with the experimental observations of Tang et al. (2024). Figure 3(d) shows the evolution of the shape factor. An inset highlights the low-Reynolds-number regime, where the RNL-WRLES results span a similar vertical range to DNS but do not follow the same detailed trend at low Re_θ. Nevertheless, the mean value $H \approx 1.43$–1.47 across all Re_D is characteristic of turbulent boundary layers, indicating that the simulations recover realistic integral flow behavior despite discrepancies in transitional evolution.

Figure 4 presents profiles of the inner-scaled streamwise component of the velocity for all trip conditions compared with DNS of spatially developing boundary layers at $Re_\theta \approx 2000$ and $Re_\theta \approx 4060$. When expressed in inner units, all cases exhibit similar behavior in the near-wall region, even at lower Reynolds numbers. Deviations arise primarily in the outer region of the boundary layer, where the mean velocity profiles show greater sensitivity to both Reynolds number and trip forcing. Consistent with Schlatter & Örlü (2012) and Kozul et al. (2016), the onset of profile collapse becomes evident at higher Reynolds numbers. The RNL-WRLES profiles collapse for $Re_\theta \geq 3030$ (not shown), which is a higher value than for the temporally developing DNS (Kozul et al., 2016) which shows comparable behavior at $Re_\theta = 1968$. The later collapse of the RNL data led to the choice of presenting re-

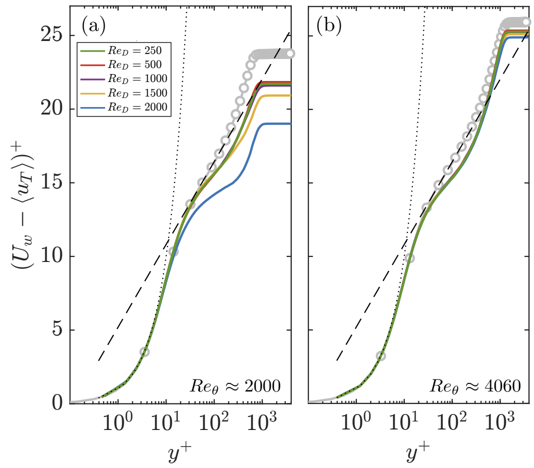

Figure 4. Inner-scaled streamwise component of the velocity at (a) $Re_\theta \approx 2000$ and (b) $Re_\theta \approx 4060$ for all Re_D. Spatially developing DNS (grey circles) have sparse data points for visualization. See figure 2 caption for legend details. Dotted line indicates $(U_w - \langle u_T \rangle)^+ = y^+$ and dashed line indicates $1/\kappa \log(y^+) + B$ with $\kappa = 0.41$ and $B = 5.2$.

sults at $Re_\theta = 2000$ rather than the $Re_\theta = 1100$ in Kozul et al. (2016). This behavior is also consistent with the skin-friction trends in figure 2, which show the RNL-WRLES transitioning later than the DNS. Larger Re_D values generate stronger initial wakes, leading to an over-excited flow state that requires a longer adjustment period before reaching a sustained turbulent regime. These observations suggest that a smaller trip diameter is more appropriate for assessing lower-Reynolds-number turbulent behavior. As the $Re_D = 250$ does not produce transition in prior DNS and exhibits different energy growth here, a trip diameter of $Re_D = 500$ provides the best balance of realistic flow excitation and fast transition to the fully developed

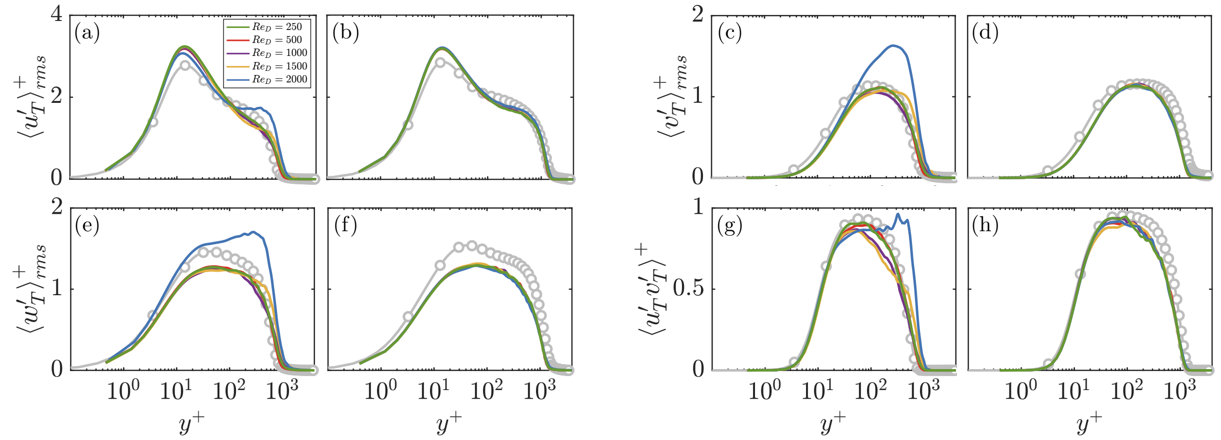

Figure 5. Inner-scaled root-mean-square (rms) of the (a,b) streamwise; (c,d) wall-normal; (e,f) spanwise components of velocity; and (g,h) the cross-plane Reynolds stresses as a function of wall-normal distance for all Re_D at (a,c,e,g) $Re_\theta \approx 2000$ and (b,d,f,h) $Re_\theta \approx 4060$. See figure 2 caption for legend details. Note the vertical axis changes for each panel set.

state.

Figure 5(a,b) presents the inner-scaled root-mean-square (rms) of the streamwise component of the velocity fluctuations as a function of wall-normal distance in inner units at two Reynolds numbers. At the lower Re_θ, $Re_D = 2000$ (the largest trip) remains within a transitional regime, leading to an increased secondary peak. As Re_θ increases, the profiles exhibit improved collapse across all Re_D. For both Reynolds numbers, $\langle u'_T \rangle^+_{rms}$ is over-predicted, a well-documented characteristic of RNL dynamics e.g., Minnick & Gayme (2024); Gayme & Minnick (2019). This excess streamwise energy is accompanied by a slight under prediction of the wall-normal fluctuation intensity $\langle v'_T \rangle^+_{rms}$ shown in figure 5(c,d) and spanwise fluctuation intensity $\langle w'_T \rangle^+_{rms}$ shown in figure 5(e,f) due to continuity. Similar to figure 5(a), $\langle v'_T \rangle^+_{rms}$ and $\langle w'_T \rangle^+_{rms}$, also exhibit the footprint of excess energy in the outer-layer of the flow for $Re_D = 2000$ at $Re_\theta = 2000$. Figure 5(g,h) displays the inner-scaled cross-plane Reynolds shear stress where similar trends are observed at $Re_\theta = 2000$, consistent with Kozul et al. (2016). As the flow develops to $Re_\theta = 4060$, all the statistics collapse.

Figure 6 shows the same quantities in figures 4 and 5(a,b), respectively $(U_w - \langle u_T \rangle)^+$ and $\langle u'_T \rangle^+_{rms}$, at fixed times $Re_t = 2.6 \times 10^5$ and $Re_t = 41.8 \times 10^5$ (i.e., the same temporal locations presented in figure 1) in analogy to fixed downstream positions in a spatially developing boundary layer. It is important to note that the profiles at each Re_t correspond to different values of Re_θ, Re_{δ^*}, and Re_τ (see figure 3). Thus, the comparison reflects the temporal evolution of the flow under different trip conditions at a common physical time, rather than a comparison at matched Reynolds numbers (as in figures 4 and 5). However, this analysis enables the isolation of the influence of the tripping device (Marusic et al., 2015; Tang et al., 2024). At the earlier time, the boundary layer is still adjusting to the disturbance introduced by the trip. By the later time, the flow has evolved substantially, and the boundary layer exhibits characteristics of a fully developed turbulent state, with reduced sensitivity to the specific trip diameter. An extended logarithmic region is observed as Re_D increases, while near the wall ($y^+ < 100$) profiles collapse even at this early stage. The wake region becomes increasingly pronounced with increasing Re_D, and the inner-layer peak decreases with trip diameter. At the later time, the profiles exhibit greater collapse, and the inner peak of $\langle u'_T \rangle^+_{rms}$ becomes more consistent across cases.

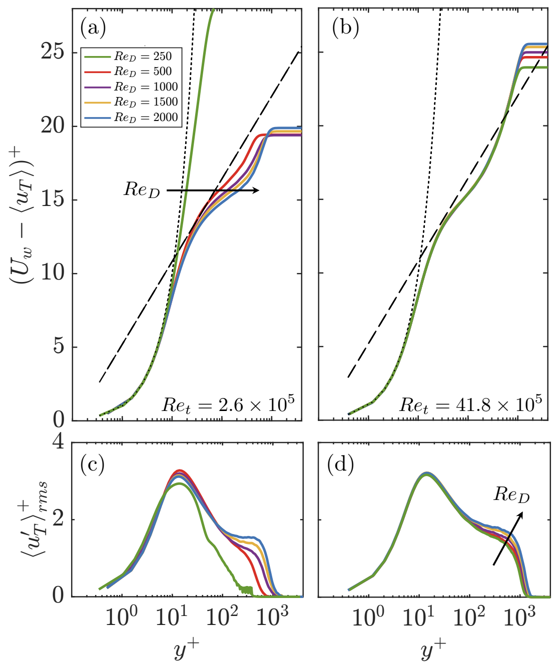

Figure 6. Inner-scaled (a,b) streamwise component of the velocity and (c,d) rms streamwise component of the velocity as a function of wall-normal distance for all Re_D at (a,c) $Re_t = 2.6 \times 10^5$ and (b,d) $Re_t = 41.8 \times 10^5$.

Although a larger wake region persists for increasing Re_D, the outer-layer peak shows improved agreement among the different trip conditions at the later time.

Figure 7 illustrates the temporal evolution of the turbulent kinetic energy (TKE) $k_T = 0.5 \langle \boldsymbol{u'_T} \cdot \boldsymbol{u'_T} \rangle$ as a function of wall-normal distance for all Re_D. As Re_D increases from 250 to 2000, the geometric modification of the trip diameter is evident across a range of wall-normal heights. These geometric variations directly influence the amplitude of the TKE and temporal evolution of the flow, as previously observed in the skin friction plots (Figure 2) . This behavior is consistent with prior experimental measurements immediately downstream of a wall-mounted elements, which show differences in the flow energy and boundary layer evolution that depend on the characteristics of the trip (Tang et al., 2024). For $Re_D = 250$ (figure 7(a)),

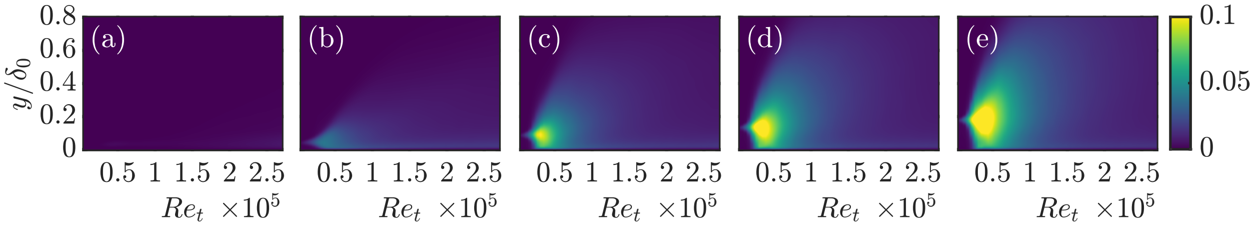

Figure 7. Turbulent kinetic energy, k_T, normalized by U_w^2 for (a) $Re_D = 250$, (b) $Re_D = 500$, (c) $Re_D = 1000$, (d) $Re_D = 1500$, and (e) $Re_D = 2000$ as a function of temporal Reynolds number and wall normal distance. The vertical and horizontal directions are cropped for visualization purposes.

the trip itself does not seem to be creating any TKE, rather the production within the developing boundary layer drives the transition (consistent with figure 2). The slightly higher production rate in RNL dynamics, see e.g., Gayme & Minnick (2019) may explain why the RNL-WRLES transitions to turbulence while the DNS does, but further analysis is needed to validate this conjecture. For $Re_D > 250$ (figure 7(b,c,d,e)), the TKE rises more sharply downstream of the trip and persists over a longer duration, indicating a prolonged influence of the trip on the flow field, again consistent with the behavior seen in Figure 2. This elevated TKE can help explain the enhanced outer-layer activity observed in the boundary layer where the secondary peak increases in $\langle u_T' \rangle^+_{rms}$ with increasing Re_D as the flow develops (seen in figure 6 (c,d)).

CONCLUSIONS

This study demonstrates that RNL-WRLES capture the essential features of the influence of trip size on the temporal development of a boundary layer over a moving wall. Larger trip diameter is shown to produce stronger early excitation, elevated turbulent kinetic energy, and a prolonged transitional regime, consistent with DNS trends. While the trip size effects the time evolution of TKE and outer-layer activity, these differences diminish as the boundary layer approaches a fully developed turbulent state. RNL-WRLES show larger initial energy amplification and a longer transition time versus DNS, but reproduce integral growth trends, the asymptotic value of the skin friction coefficient, and accurate statistical features in the low-to-moderate Reynolds number regime. These results suggest the promise of RNL-WRLES as a computationally efficient yet physically meaningful framework to analyze the mechanisms by which trip wire characteristics influence boundary layer transition and development.

ACKNOWLEDGMENTS

Computations were performed at the Advanced Research Computing at Hopkins (ARCH) core facility (rockfish.jhu.edu) originally supported by the US National Science Foundation (NSF). Partial support is from the in-house Laboratory Independent Research program, Problem Element 0601153N, managed by the NSWC Carderock Division Office of Technology and Innovation for the Office of Naval Research. A. C. Risha also acknowledges support from the Department of Defense (DoD) through the National Defense Science and Engineering Graduate (NDSEG) fellowship program.

REFERENCES

Bretheim, J. U., Meneveau, C. & Gayme, D. F. 2018 A restricted nonlinear large eddy simulation model for high reynolds number flows. J. Turbulence **19** (2), 141–166.

Eitel-Amor, G., Örlü, R. & Schlatter, P. 2014 Simulation and validation of a spatially evolving turbulent boundary layer up to $Re_\theta = 8300$. Int'l J. Heat and Fluid Flow **47**, 57–69.

Gayme, D. F. & Minnick, B. A. 2019 Coherent structure-based approach to modeling wall turbulence. Phys. Rev. Fluids **4** (11), 110505.

Kozul, M., Chung, D. & Monty, J. P. 2016 Direct numerical simulation of the incompressible temporally developing turbulent boundary layer. J. Fluid Mech. **796**, 437–472.

Marusic, I., Chauhan, K. A., Kulandaivelu, V. & Hutchins, N. 2015 Evolution of zero-pressure-gradient boundary layers from different tripping conditions. J. Fluid Mech. **783**, 379–411.

Minnick, B. A. & Gayme, D. F. 2024 Restricted nonlinear boundary layers over a moving wall. In Int'l Symposium on Turbulence and Shear Flow Phenomena (TSFP-13).

Minnick, B. A., Viggiano, Bianca & Gayme, D. F. 2023 Augmented restricted nonlinear (ARNL) model for high Reynolds number wall-turbulence. In Conf. on Interdisciplinary Turbulence Initiative, pp. 65–75.

Nicoud, F. & Ducros, F. 1999 Subgrid-scale stress modelling based on the square of the velocity gradient tensor. Flow, Turbulence and Combustion **62** (3), 183–200.

Park, J., Hwang, W. & Rhee, S. H. 2024 Experimental investigation of boundary layer transition by wall-mounted elements. Phys. Fluids **36** (4), 044113.

Risha, A. C., Minnick, B. A. & Gayme, D. F. 2026 Restricted nonlinear investigation of developing boundary layers over decelerating walls. In Conf. on Interdisciplinary Turbulence Initiative, p. 012015.

Schlatter, P., Li, Q., Brethouwer, G., Johansson, A. V. & Henningson, D. S. 2010 Simulations of spatially evolving turbulent boundary layers up to $Re_\theta = 4300$. Int'l J. Heat Fluid Flow **31** (3), 251–261.

Schlatter, P. & Örlü, R. 2012 Turbulent boundary layers at moderate Reynolds numbers: inflow length and tripping effects. J. Fluid Mech. **710**, 5–34.

Smits, A. J., Matheson, N. & Joubert, P. N. 1983 Low-reynolds-number turbulent boundary layers in zero and favorable pressure gradients. J. Ship Research **27**, 147–157.

Tang, Z., Jiang, N., Lu, Z. & Zhou, Q. 2024 Artificially thickened boundary layer turbulence due to trip wires of varying diameter. Phys. Rev. Fluids **9** (2), 024606.

Thomas, V. L., Farrell, B. F., Ioannou, P. J. & Gayme, D. F. 2015 A minimal model of self-sustaining turbulence. Phys. Fluids **27** (10), 105104.

Watanabe, T., Zhang, Xi. & Nagata, K. 2019 Direct numerical simulation of incompressible turbulent boundary layers and planar jets at high Reynolds numbers initialized with implicit large eddy simulation. Computers & Fluids **194**, 104314.